Supplementary Information for

Protonated portlandite precursor unlocks enhanced nucleation and growth for cement hydration

Jingyi Zeng[1], Qiao Liu[1], Jin Yang[1,*], Zhongyong Zhang[2], Huangjie Zou[2], Ying Su[1], Yingbin Wang[1], Yubo Li[1], Neng Li[2,*] & Xingyang He[1,*]

[1]School of Civil Engineering, Architecture and Environment, Hubei University of Technology, Wuhan 430068, China.

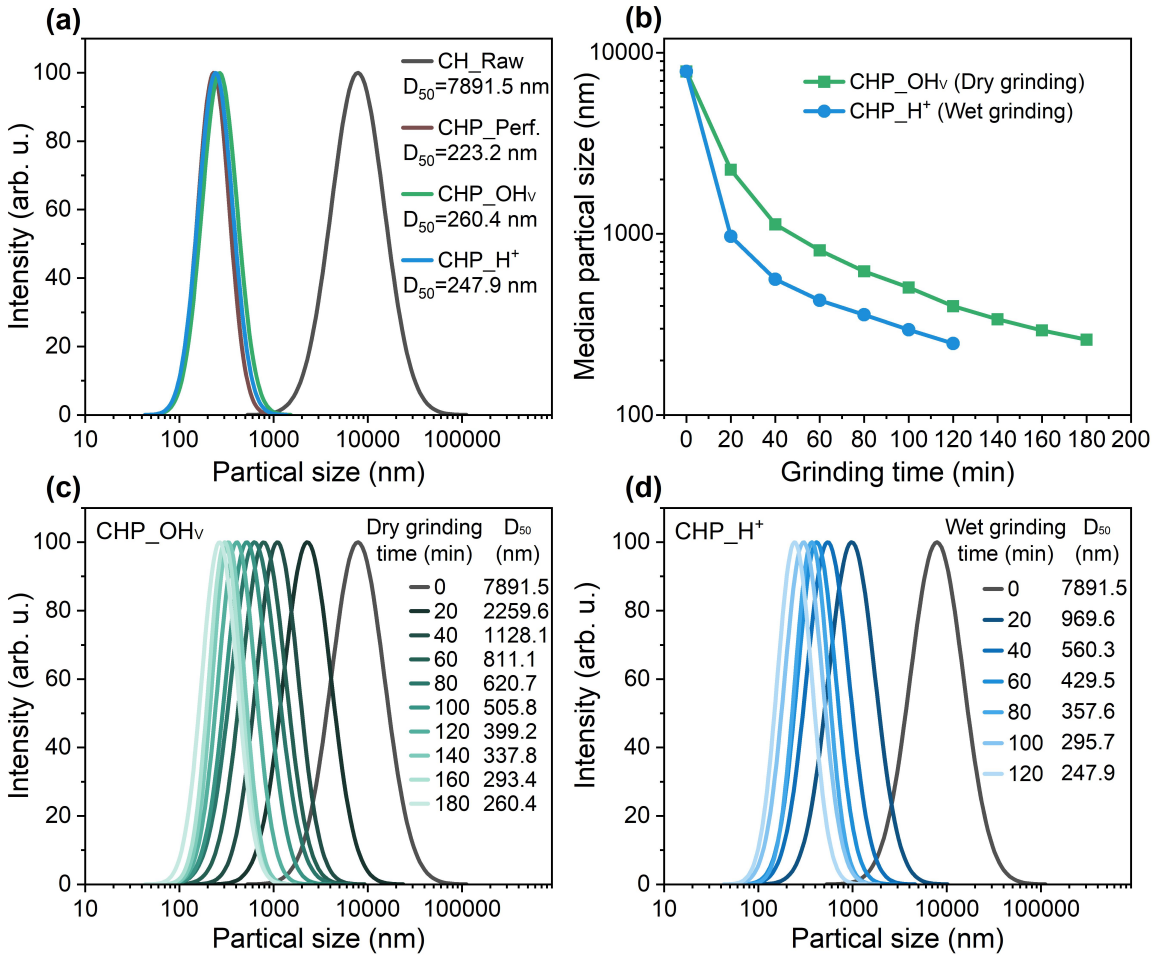
[2]State Key Laboratory of Silicate Materials for Architectures, Wuhan University of Technology, Wuhan 430070, China.

[*]Corresponding author: jinyang@hbut.edu.cn, lineng@whut.edu.cn, hexycn@163.com

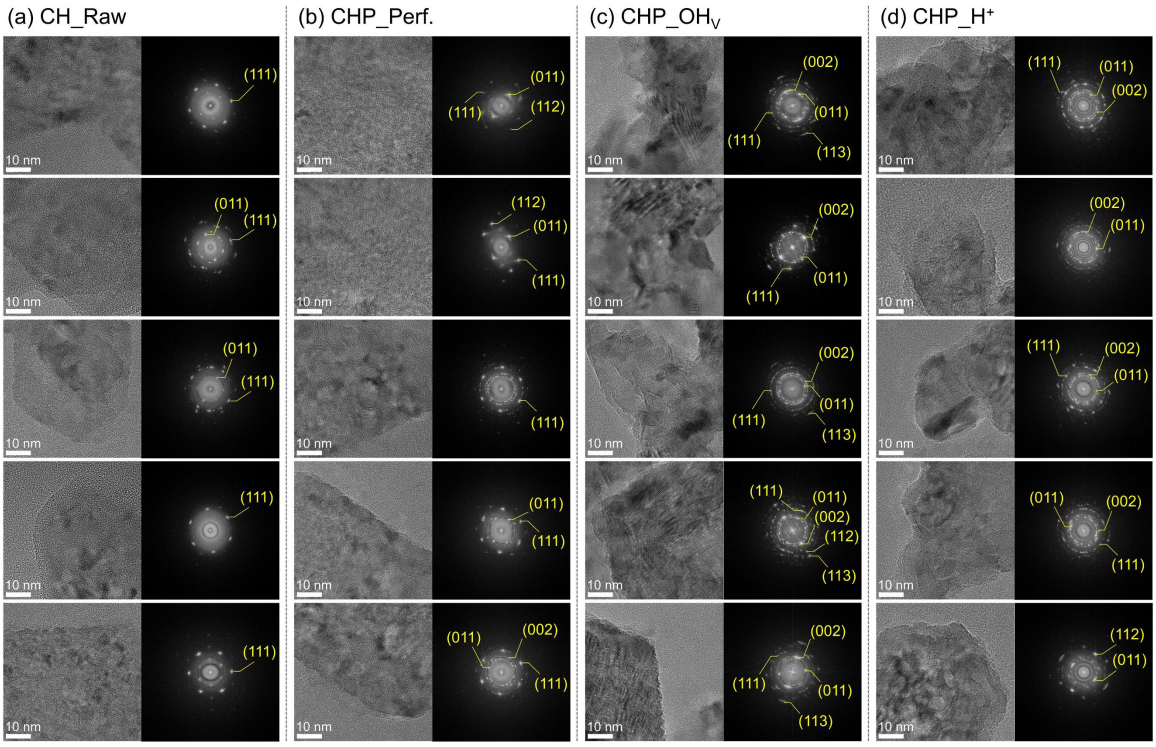
Content

Supplementary Fig. 1 | Particle size of the four types of CH..... 4
Supplementary Fig. 2 | Microstructure and crystallographic features of four types of CH...
..... 5
Supplementary Fig. 3 | Static settlement evaluation of slurry stability for four CH types....
..... 6
Supplementary Fig. 4 | Electrical conductivity of four CH types.....7
Supplementary Fig. 5 | Auger electron energy dispersive spectroscopy (O *KL1*) spectra for four CH types..... 8
Supplementary Fig. 6 | Experimental flowchart for the preparation of CHP_OH_V and CHP_H^+..... 9
Supplementary Fig. 7 | Crystallographic parameters in the XRD spectra of the four types of CH..... 10
Supplementary Fig. 8 | Crystal structure models of two types of CH..... 11
Supplementary Fig. 9 | H_2O adsorption/desorption isotherms of CHP_Perf., CHP_OH_V and CHP_H^+..... 12
Supplementary Fig. 10 | Raman spectra of the samples after two cycles of D_2O adsorption and desorption.....13
Supplementary Fig. 11 | In-situ Raman spectra and -OD peak quantification..... 14
Supplementary Fig. 12 | In-situ XPS O 1*s* spectra and deconvoluted peak (O_V, O_A, and O_P) percentages.....15
Supplementary Fig. 13 | The trend of normalized XPS O 1*s* spectra for CH under different treatment conditions.....16
Supplementary Fig. 14 | Thermogravimetry weight loss of the C-S-H gel..... 17
Supplementary Fig. 15 | Photograph of different CHP in cement pore solution at different time points..... 18
Supplementary Fig. 16 | Compressive strength of cement pastes at different curing ages
..... 19
Supplementary Fig. 17 | Thermal weight loss of C-S-H gel, AFt and CH in cement pastes at different curing ages..... 20
Supplementary Fig. 18 | X-ray diffraction patterns of cement pastes at different curing

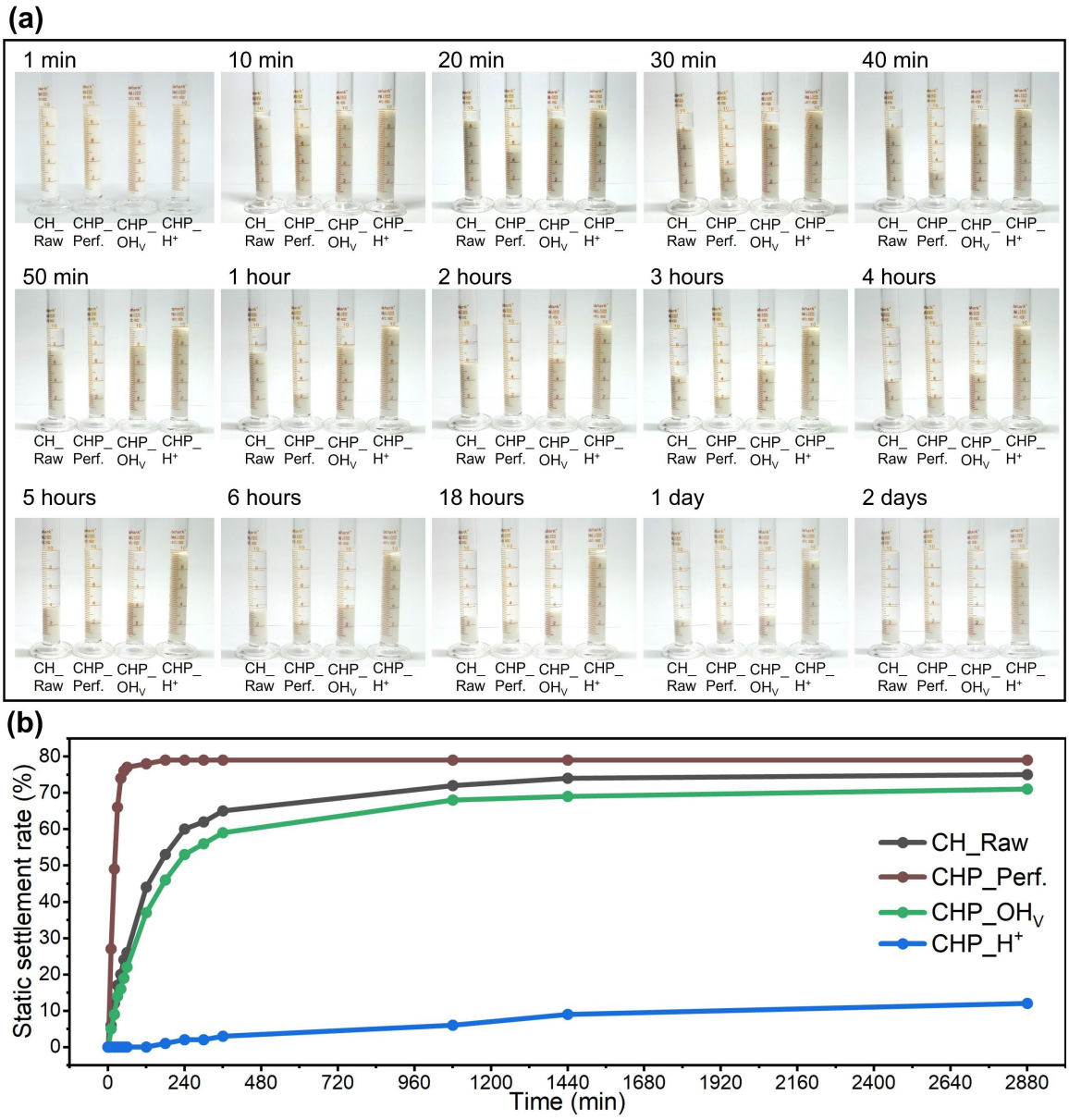
ages..... 21
Supplementary Fig. 19 | Pore structure characterization of cement pastes..... 22
Supplementary Fig. 20 | Experimental elastic modulus frequency and theoretical probability density function of cement pastes at 28 days..... 23
Supplementary Fig. 21 | The proportion of each phase component, based on the deconvoluted results of theoretical frequency counts.....24
Supplementary Fig. 22 | Growth rate of compressive strength.....25
Supplementary Fig. 23 | SEM-EDS surface scan images and element distribution maps of CH in conventional cement paste at 28 days..... 26
Supplementary Fig. 24 | Preparation process for cement paste with reserved artificial micropores..... 27
Supplementary Fig. 25 | SEM-EDS surface scan images and element distribution maps of AFt/AFm and CH in cement paste at 28 days..... 28
Supplementary Fig. 26 | SEM-EDS surface scan images and element distribution maps of CH in cement paste containing artificial micropores at 28 days..... 29
Supplementary Fig. 27 | Characterisation of Ordinary Portland cement (P.O. 42.5 type).....
..... 30
Supplementary Fig. 28 | Preparation process of CHP_H^+ and schematic diagram of wet grinding process.....31
Supplementary Fig. 29 | Relationship between fractal dimension and $\log(V_n^{1/3} r_n^{-1})$, and relationship between fractal dimension and pore diameter.....32
Supplementary Fig. 30 | Convergence of the metadynamics simulations..... 33
Supplementary References..... 34



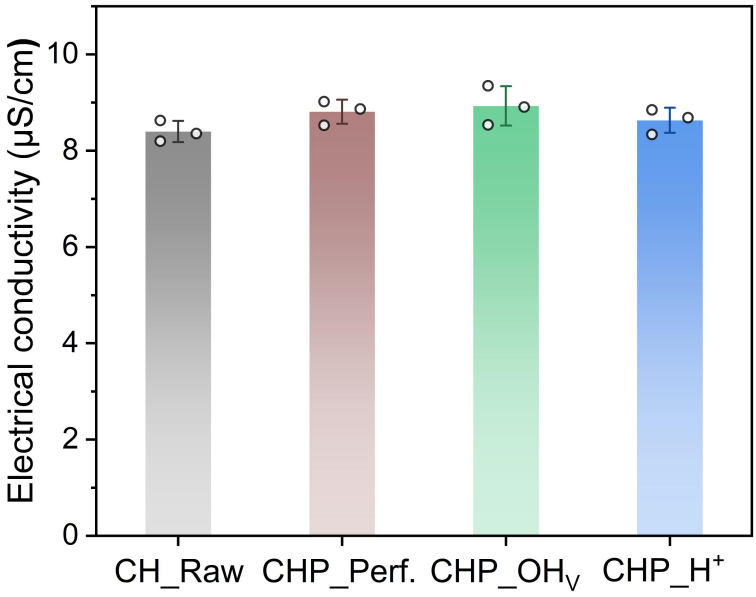
Supplementary Fig. 1 | Particle size of the four types of CH. (a) Particle size distribution and median particle size (D_{50}) for CH_Raw, CHP_Perf., CHP_OH_V and CHP_H^+. (b) Median particle size of CHP_OH_V and CHP_H^+ at different grinding times. (c) Particle size distribution of CHP_OH_V at different grinding times. (d) Particle size distribution of CHP_H^+ at different grinding times. Source data are provided as a Source Data file.



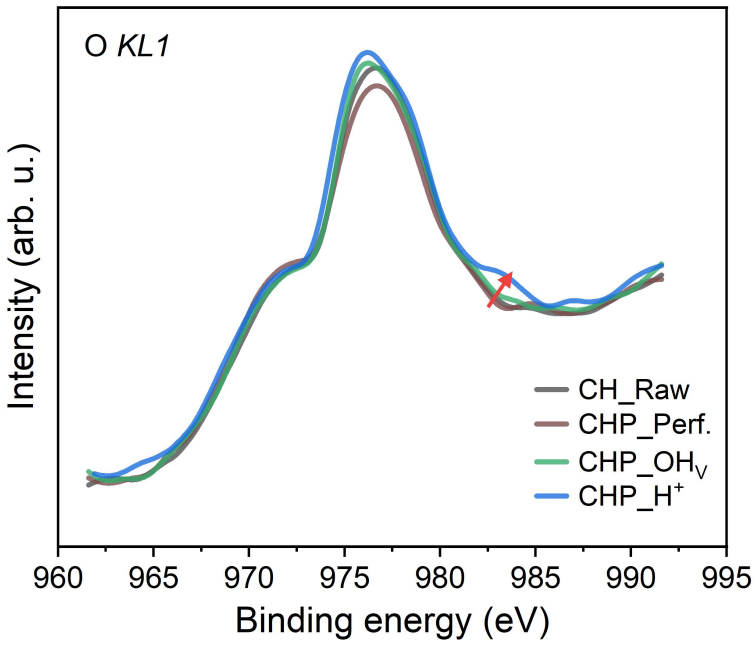
Supplementary Fig. 2 | Microstructure and crystallographic features of four types of CH. Transmission electron microscopy (TEM) images and their corresponding fast Fourier transform (FFT) images of (a) CH_Raw, (b) CHP_Perf., (c) CHP_OH_V, and (d) CHP_H^+. Scale bar, 10 nm.



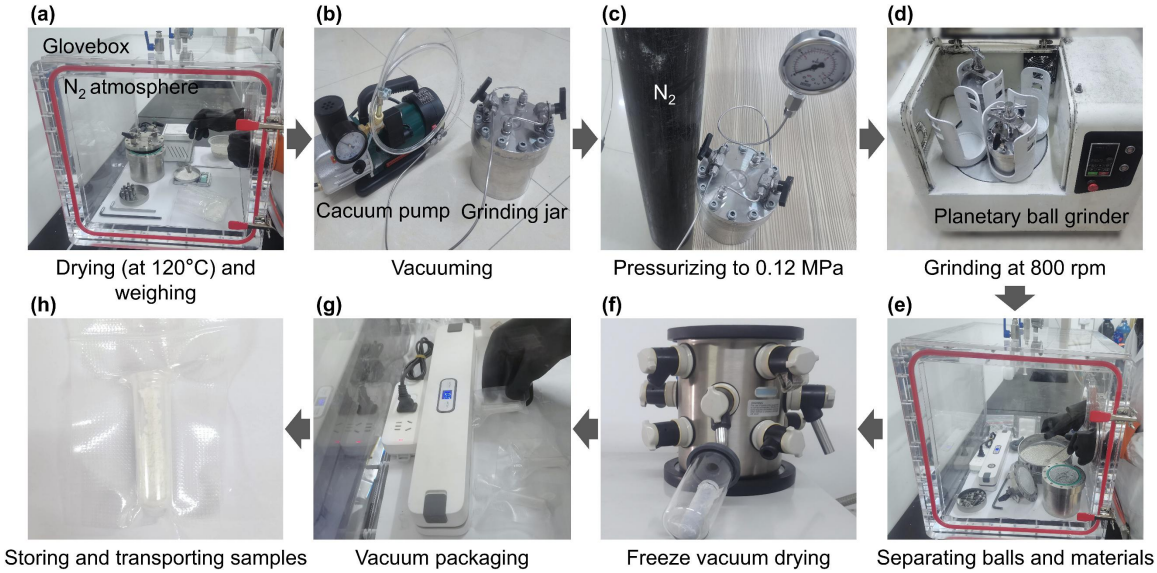
Supplementary Fig. 3 | Static settlement evaluation of slurry stability for four CH types. (a) Photograph of slurries (water/CH = 20/1) prepared from 4 types of CH at different settling times. (b) Static settlement rate curves of 4 types of CH at different settling times. Source data are provided as a Source Data file.



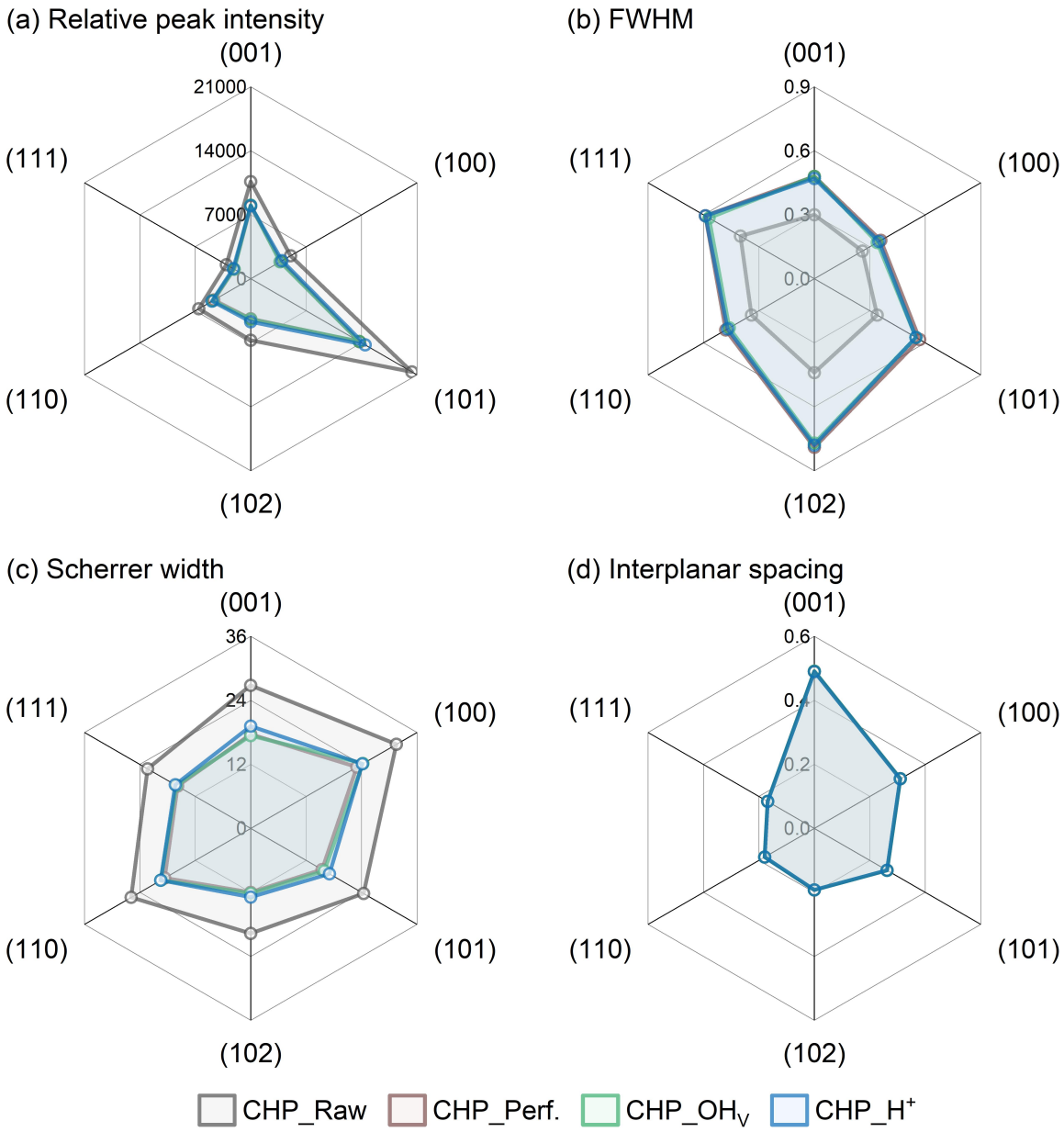
Supplementary Fig. 4 | Electrical conductivity of four CH types. All samples are tested in slurry state with a water/CH ratio of 20/1, including CH_Raw, CHP_Perf., CHP_OH_V and CHP_H^+. Data are presented as mean values, error bars represent standard deviations, with n = 3 independent replicates. Source data are provided as a Source Data file.



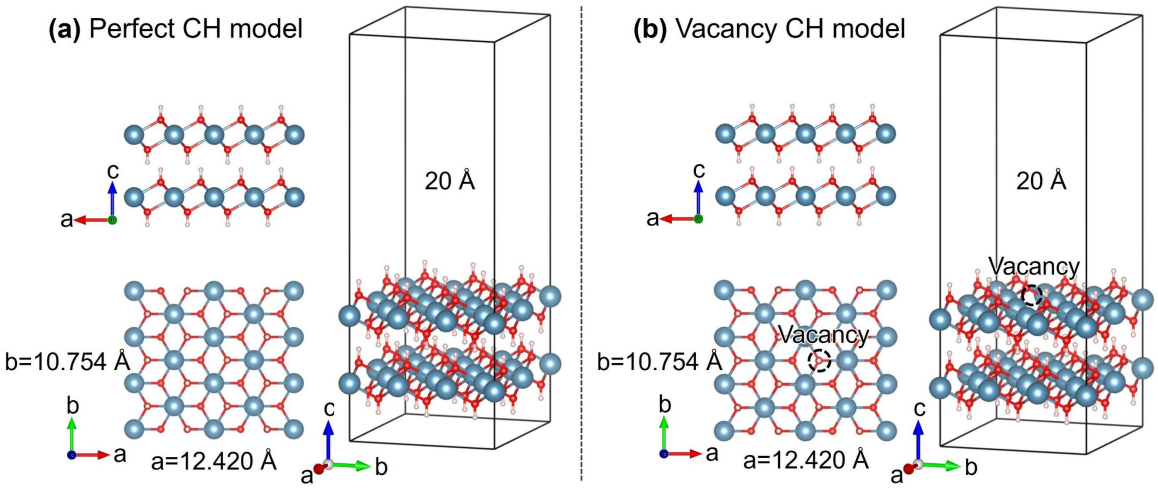
Supplementary Fig. 5 | Auger electron energy dispersive spectroscopy (O *KL1*) spectra for four CH types. Auger electron energy dispersive spectroscopy at the O *KL1* transition is tested across CH_Raw, CHP_Perf., CHP_OH_V and CHP_H^+. Source data are provided as a Source Data file.



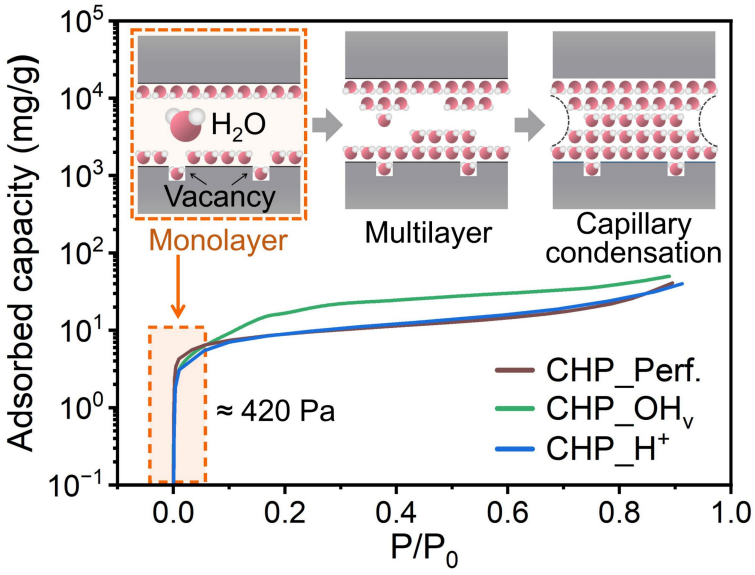
Supplementary Fig. 6 | Experimental flowchart for the preparation of CHP_OH_V and CHP_H^+. (a) Drying and weighing of CH samples in a glove box under N_2 atmosphere. For CHP_OH_V samples, CH_Raw, grinding balls, and grinding jars must each undergo heating and drying at 120°C for 30 min. (b) Vacuuming of the grinding jar. The purpose is to remove residual water and CO_2 from the internal piping of the grinding tank during CHP_OH_V preparation. (c) Pressurizing of the grinding jar. This prevents the grinding jar from drawing in air during the grinding process. (d) Grinding treatment. During operation, cold air is continuously introduced for cooling. (e) Separation of grinding balls from materials in a glove box under N_2 atmosphere. (f) Freeze vacuum drying process. Only CHP_H^+ slurry was required. CHP_H^+ slurry was sealed into test tubes within a glove box, then frozen for 6 hours followed by freeze vacuum drying for 48 hours. Finally, CHP_H^+ was dried on a heating plate for 30 min in a glove box under N_2 atmosphere. (g) Vacuum packaging in a glove box under N_2 atmosphere. Prior to this, CH_Raw and CHP_Perf. will be heated and dried at 120°C for 30 minutes. (h) Storage and transport of samples.



Supplementary Fig. 7 | Crystallographic parameters in the XRD spectra of the four types of CH. (a) Relative peak intensity. (b) Full width at half maximum (FWHM). (c) Scherrer width. (d) Interplanar spacing. These results are processed based on the XRD data in Fig. 2h. Source data are provided as a Source Data file.

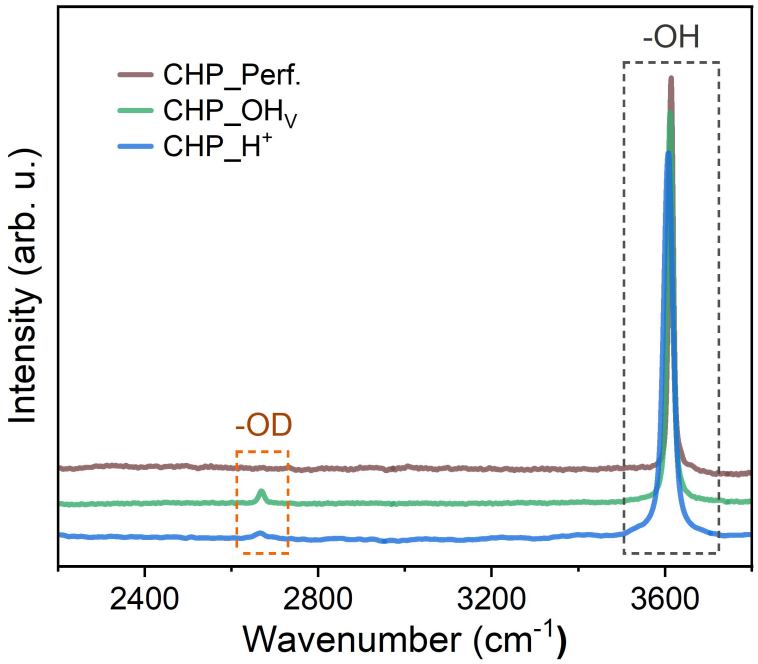


Supplementary Fig. 8 | Crystal structure models of two types of CH. (a) Perfect CH model. (b) Vacancy CH model. The figure presents multi-orientation views of the atomic arrangements, with detailed lattice parameters annotated.

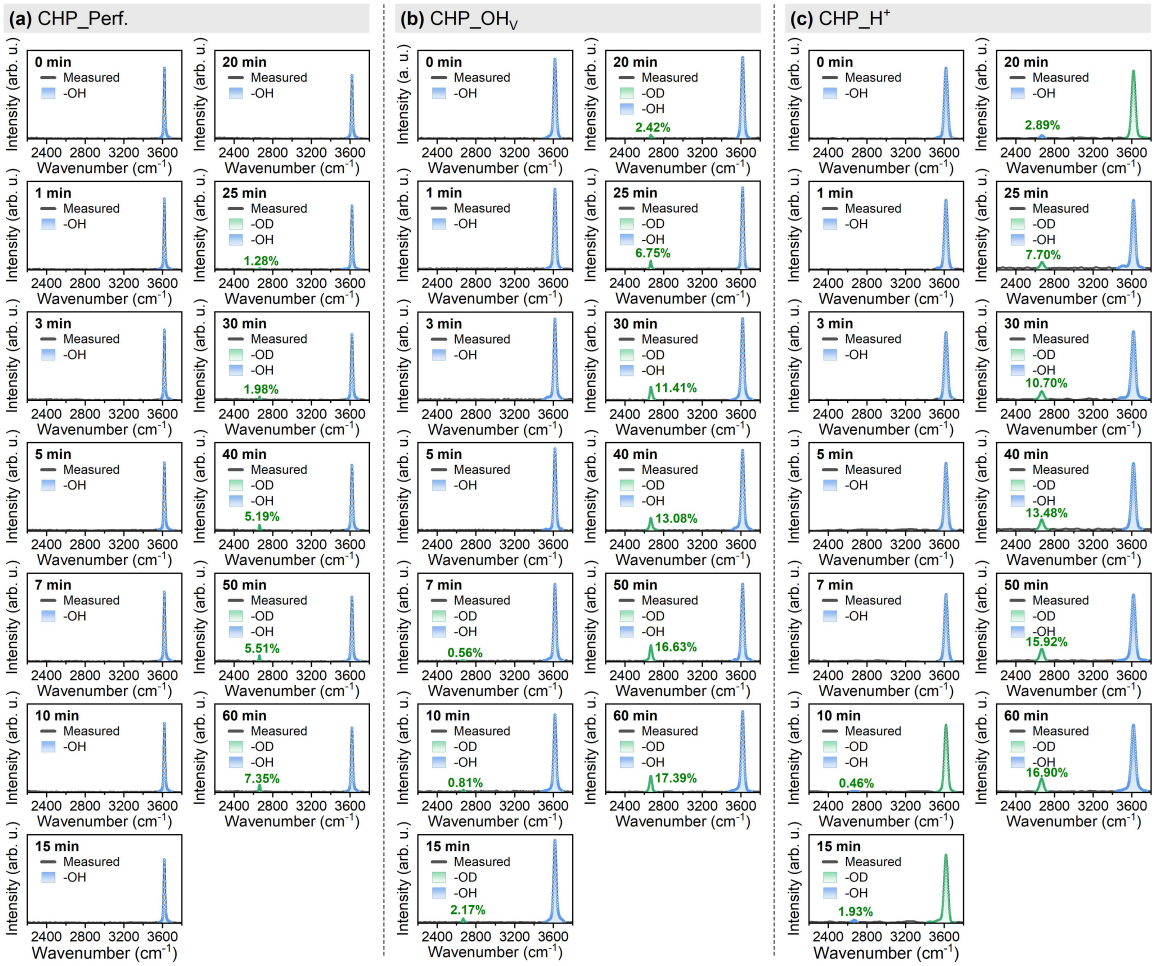


Supplementary Fig. 9 | H_2O adsorption/desorption isotherms of CHP_Perf., CHP_OH_V and CHP_H^+. The maximum pressure is about 6638.4 Pa. Source data are provided as a Source Data file.

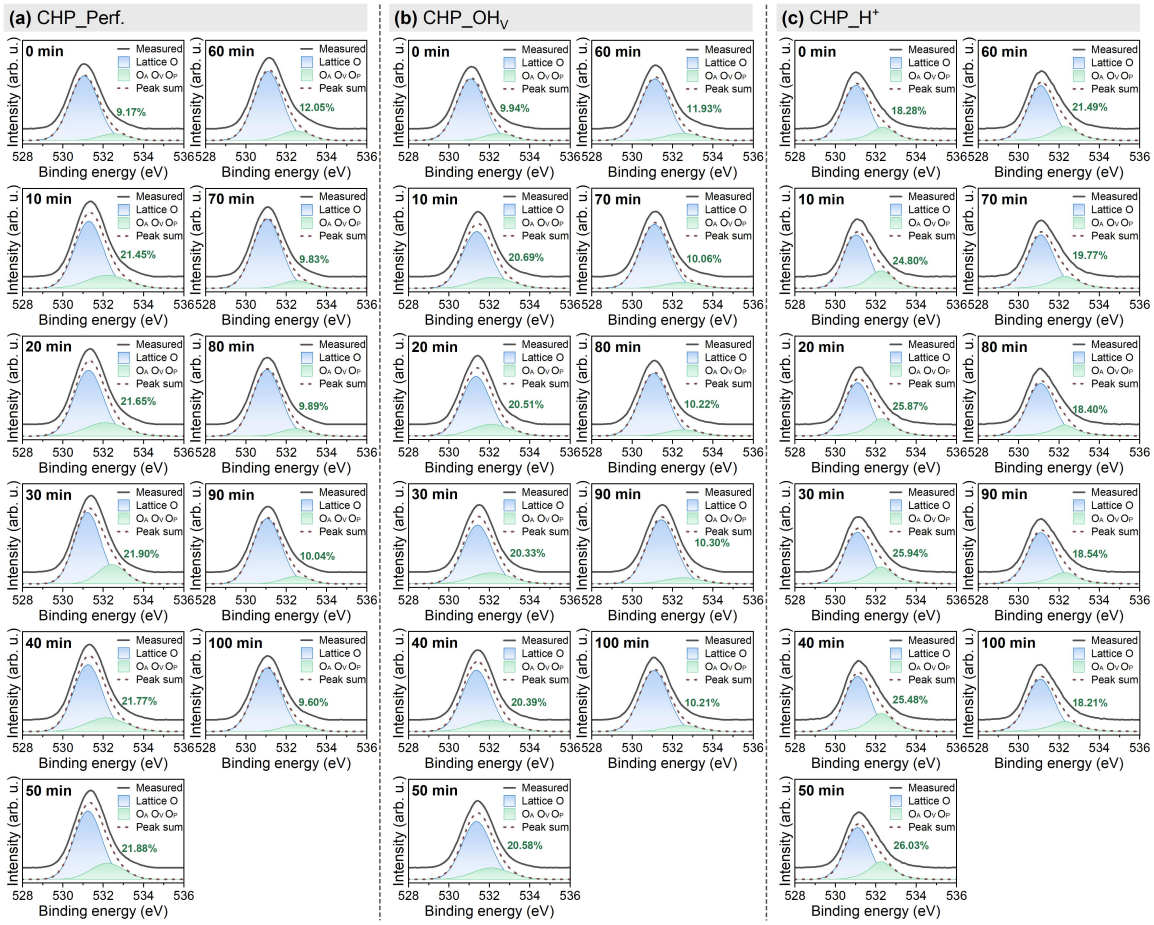
Note: The schematic diagram above the curve shows the three stages of H_2O adsorption on the CH surface: monolayer adsorption, multilayer adsorption, and capillary condensation [1, 2]. Monolayer water adsorption cannot provide sufficient water molecules to solvate ions and support ion transport, thus no bulk dissolution and ionization occur.



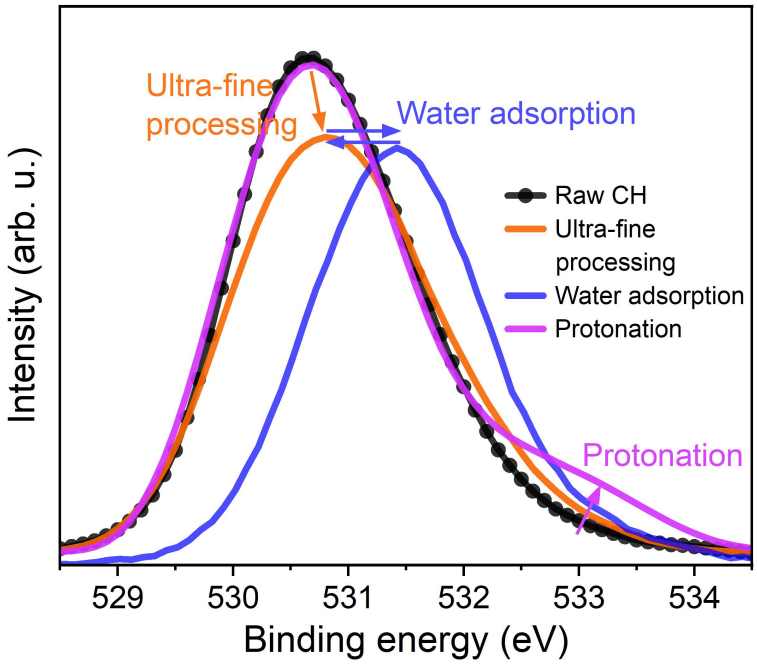
Supplementary Fig. 10 | Raman spectra of the samples after two cycles of D_2O adsorption and desorption. The samples used were those recycled as shown in Fig. 4b-d. The internal stretching vibrations involving -OH and -OD occur at 3617 cm^{-1} and 2664 cm^{-1}, respectively. Source data are provided as a Source Data file.



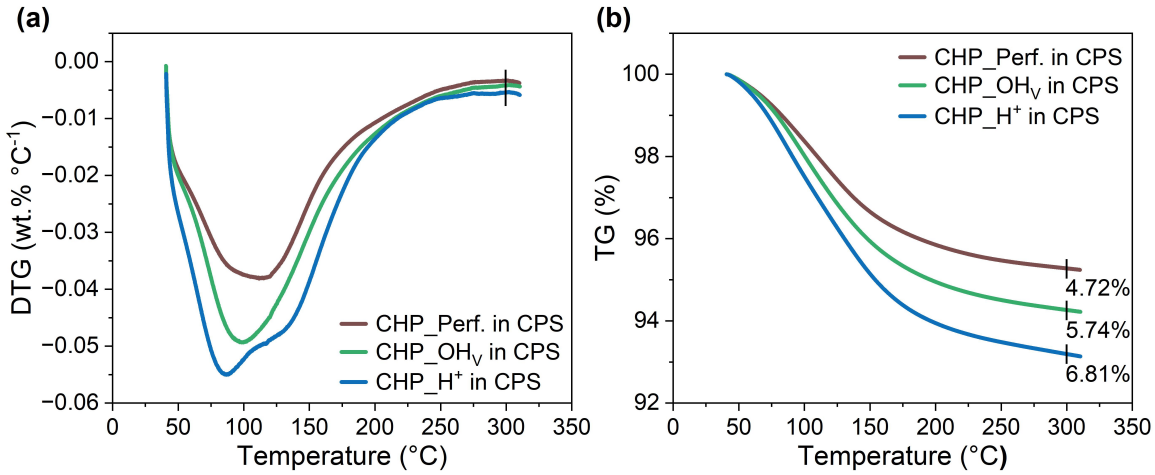
Supplementary Fig. 11 | In-situ Raman spectra and -OD peak quantification. Three sample types are characterized via in-situ Raman spectroscopy, with spectra of (a) CHP_Perf., (b) CHP_OH_V and (c) CHP_H^+. The A_{1g} (internal stretching vibrations) peaks of $Ca(OH)_2$ and $Ca(OD)_2$ are located at 3617 cm^{-1} and 2664 cm^{-1} respectively. The deconvoluted -OD peak percentages are calculated. Source data are provided as a Source Data file.



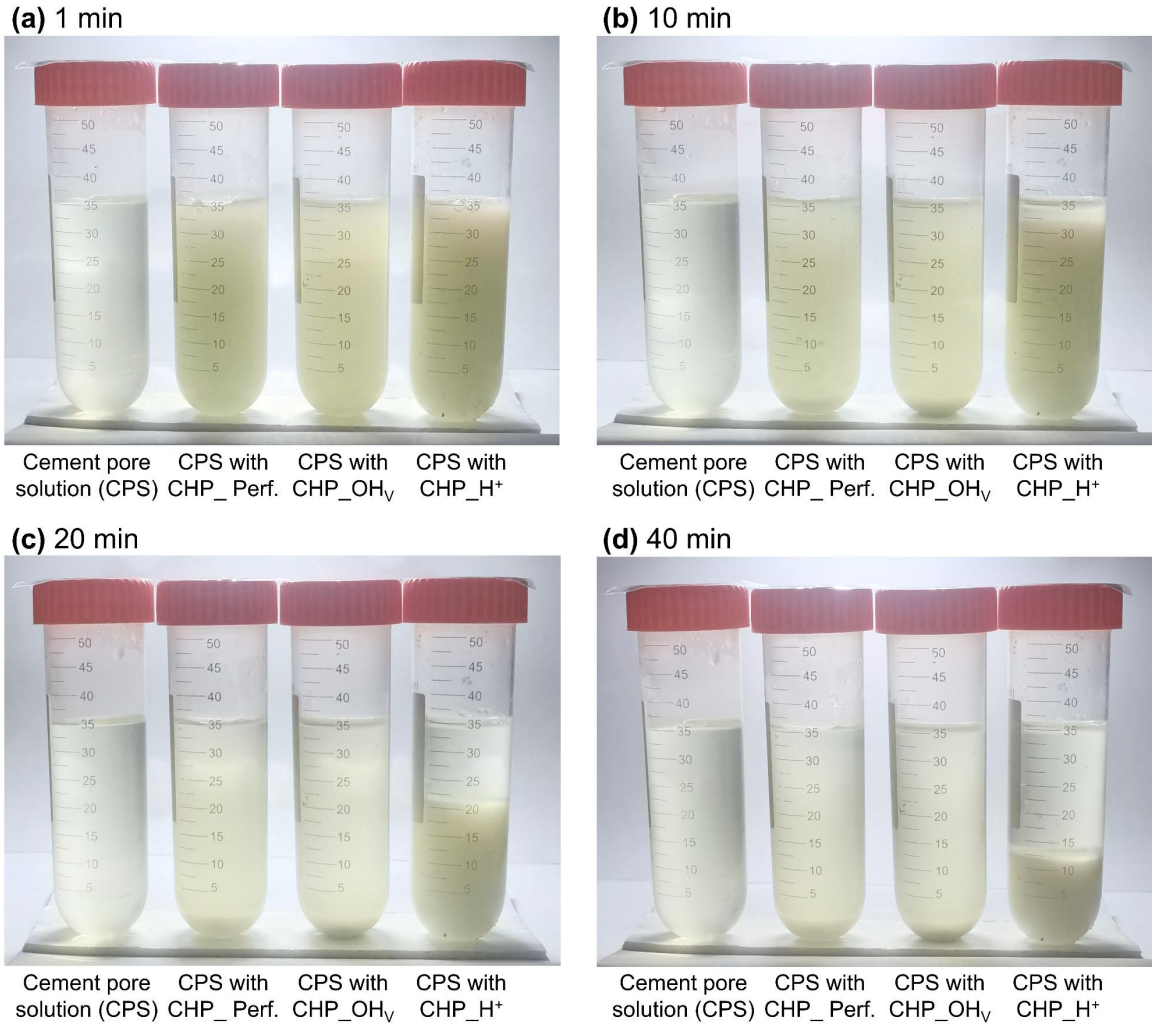
Supplementary Fig. 12 | In-situ XPS O 1*s* spectra and deconvoluted peak (O_V, O_A, and O_P) percentages. Three sample types are characterized via in-situ XPS measurement, with O 1s spectra of (a) CHP_Perf., (b) CHP_OH_V and (c) CHP_H^+. All spectra were acquired during a two-stage in-situ treatment: 50 min H_2O vapor atmosphere exposure and subsequent 50 min heating at 120°C. The percentage of three deconvoluted oxygen peaks (O_V, O_A, and O_P) is quantified via spectral fitting. Source data are provided as a Source Data file.



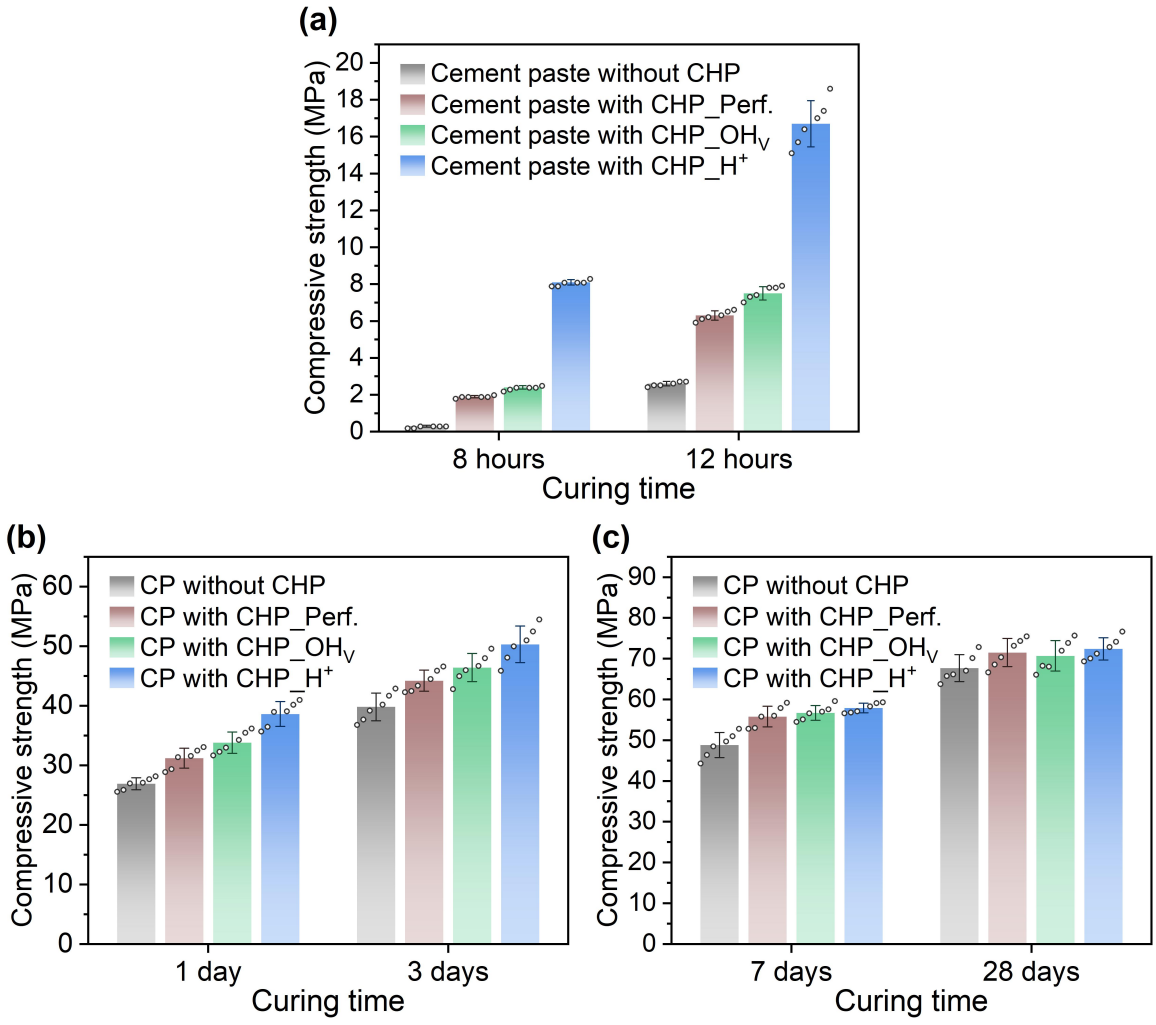
Supplementary Fig. 13 | The trend of normalized XPS O 1*s* spectra for CH under different treatment conditions. The 533.6 eV shoulder peak is unrelated to structural defects or adsorbed water, and normalized spectral evidence verifies that it originates from O_P oxygen formed during protonation. Source data are provided as a Source Data file.



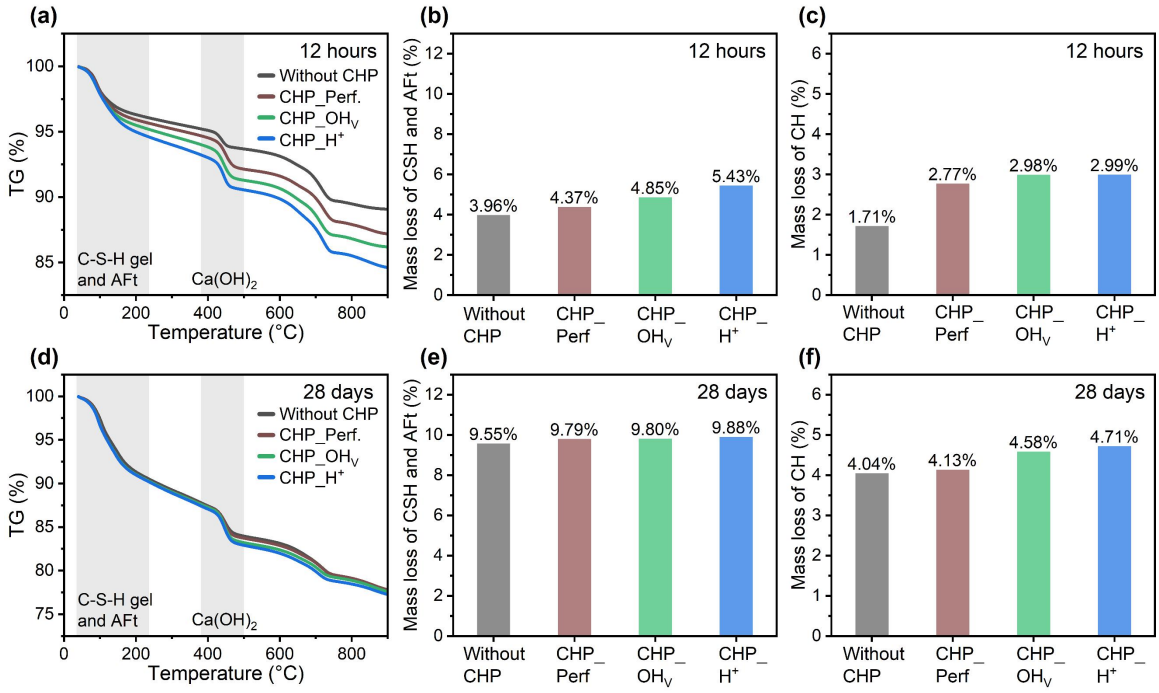
Supplementary Fig. 14 | Thermogravimetry weight loss of the C-S-H gel. (a) Derivative thermogravimetry (DTG) curve. (b) Thermogravimetry (TG) curve. All specimens were immersed in cement pore solution for 12 h followed by vacuum drying. Source data are provided as a Source Data file.



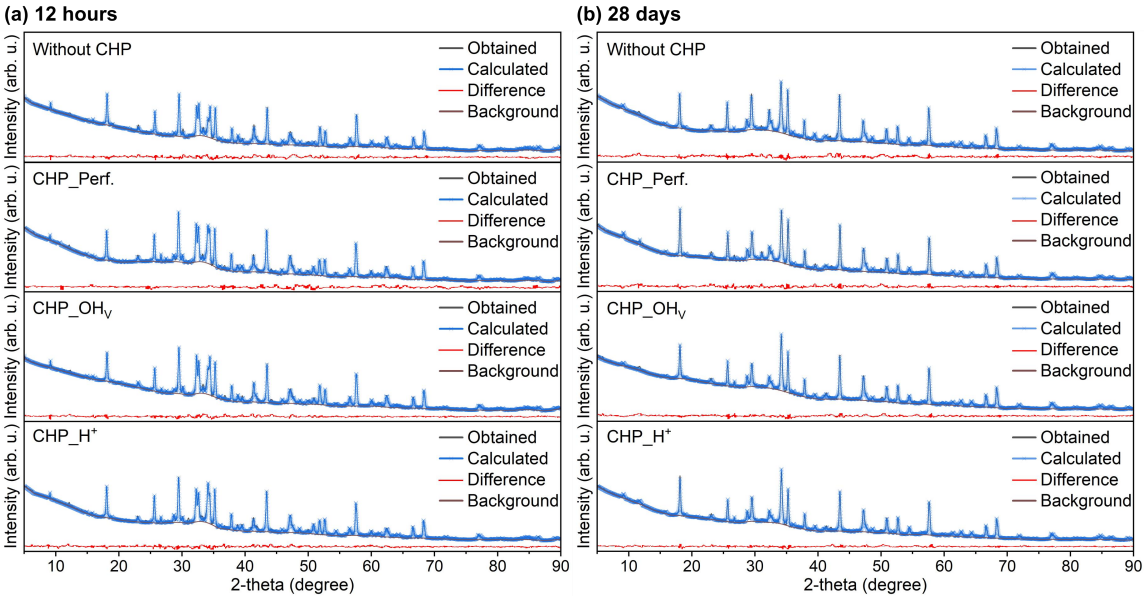
Supplementary Fig. 15 | Photograph of different CHP in cement pore solution at different time points. (a) 1 min, (b) 10 min, (c) 20 min, and (d) 40 min. The mass ratio of CHP to the pore solution is 1:200.



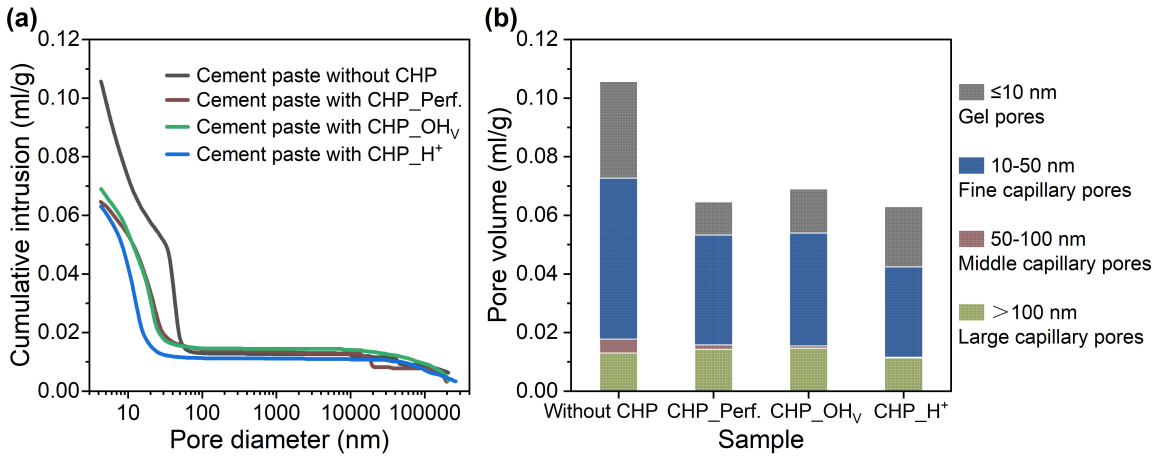
Supplementary Fig. 16 | Compressive strength of cement pastes at different curing ages. (a) 8 hours and 12 hours. (b) 1 day and 3 days. (c) 7 days and 28 days. Data are presented as mean values, error bars represent standard deviations, with n = 6 independent replicates. Source data are provided as a Source Data file.



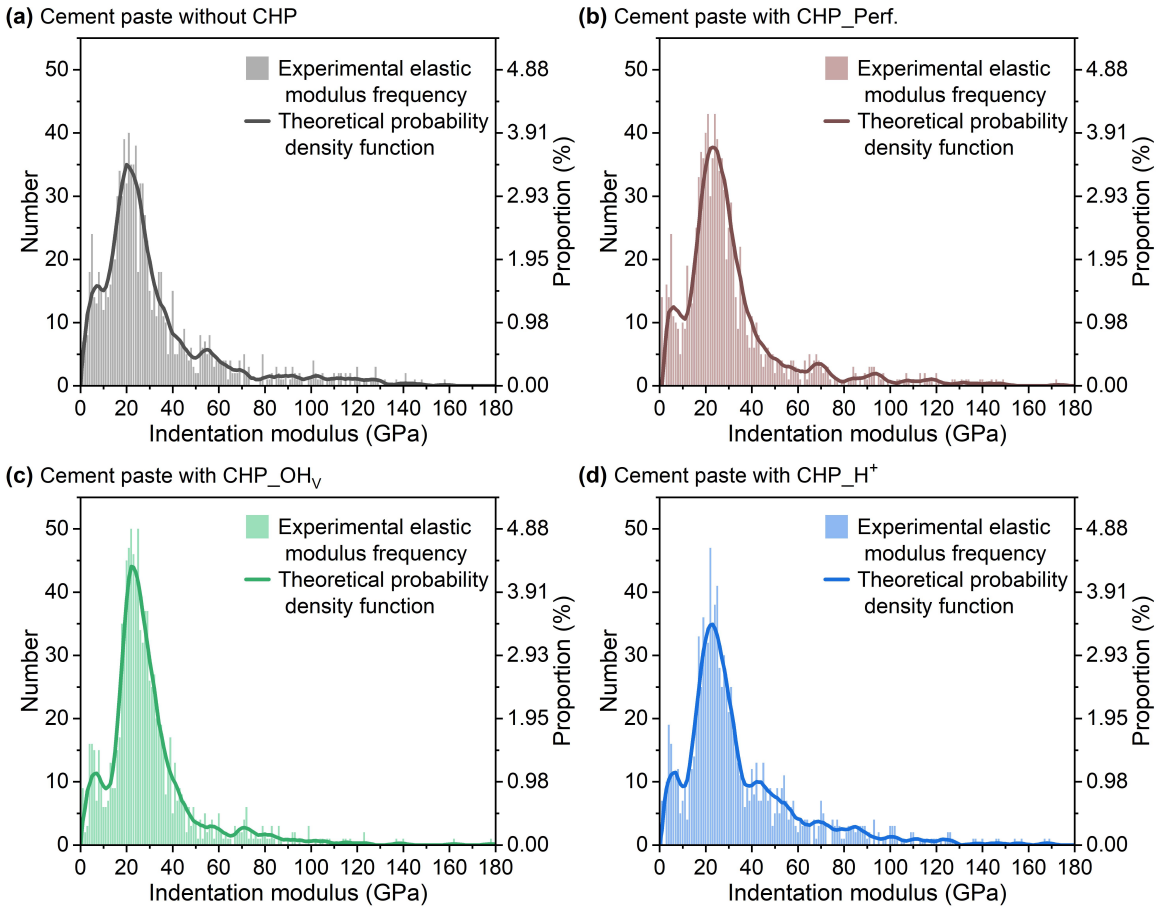
Supplementary Fig. 17 | Thermal weight loss of C-S-H gel, AFt and CH in cement pastes at different curing ages. Thermogravimetry curves of cement pastes at (a) 12 hours and (d) 28 days. Mass loss of C-S-H gel and AFt at (b) 12 hours and (e) 28 days. Mass loss of CH at (c) 12 hours and (f) 28 days. Source data are provided as a Source Data file.



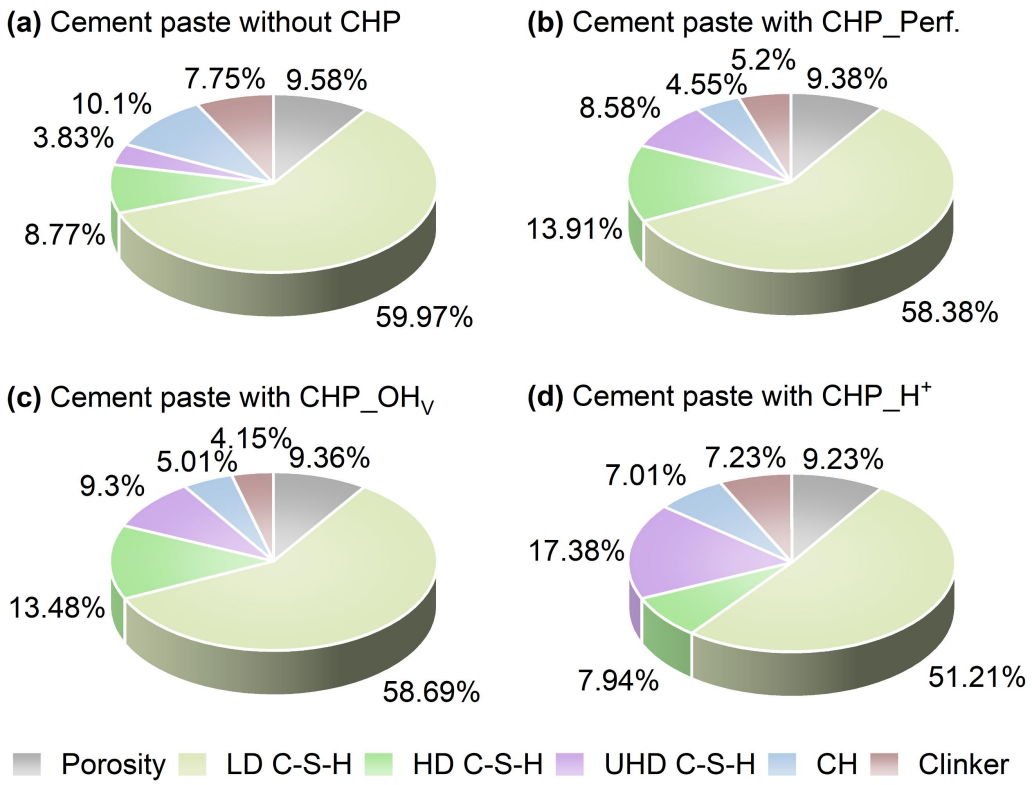
Supplementary Fig. 18 | X-ray diffraction patterns of cement pastes at different curing ages. (a) 12 hours. (b) 28 days. XRD profiles of four paste systems are refined by the Rietveld method. Quantitative Rietveld refinement is calibrated using the mass loss data of C-S-H gel, AFt and CH from Supplementary Fig. 17. Alumina was used as an internal standard, and its content accounted for 20% of the total mass. Source data are provided as a Source Data file.



Supplementary Fig. 19 | Pore structure characterization of cement pastes. (a) Cumulative mercury intrusion curve of cement pastes at 28 days. (b) Pore volume distribution of cement pastes at 28 days. Source data are provided as a Source Data file.

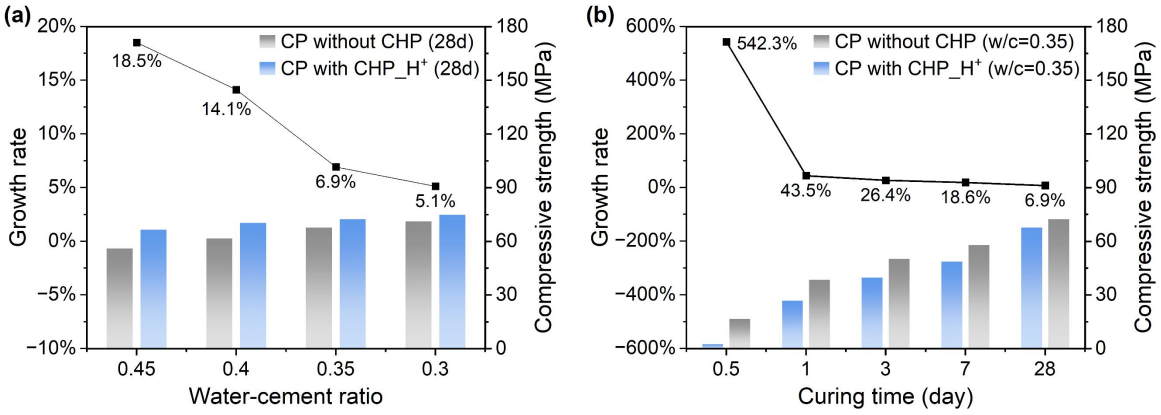


Supplementary Fig. 20 | Experimental elastic modulus frequency and theoretical probability density function of cement pastes at 28 days. (a) Cement paste without CHP. (b) Cement paste with CHP_Perf. (c) Cement paste with CHP_OH_V. (d) Cement paste with CHP_H^+. The bar size is 1 GPa. Source data are provided as a Source Data file.



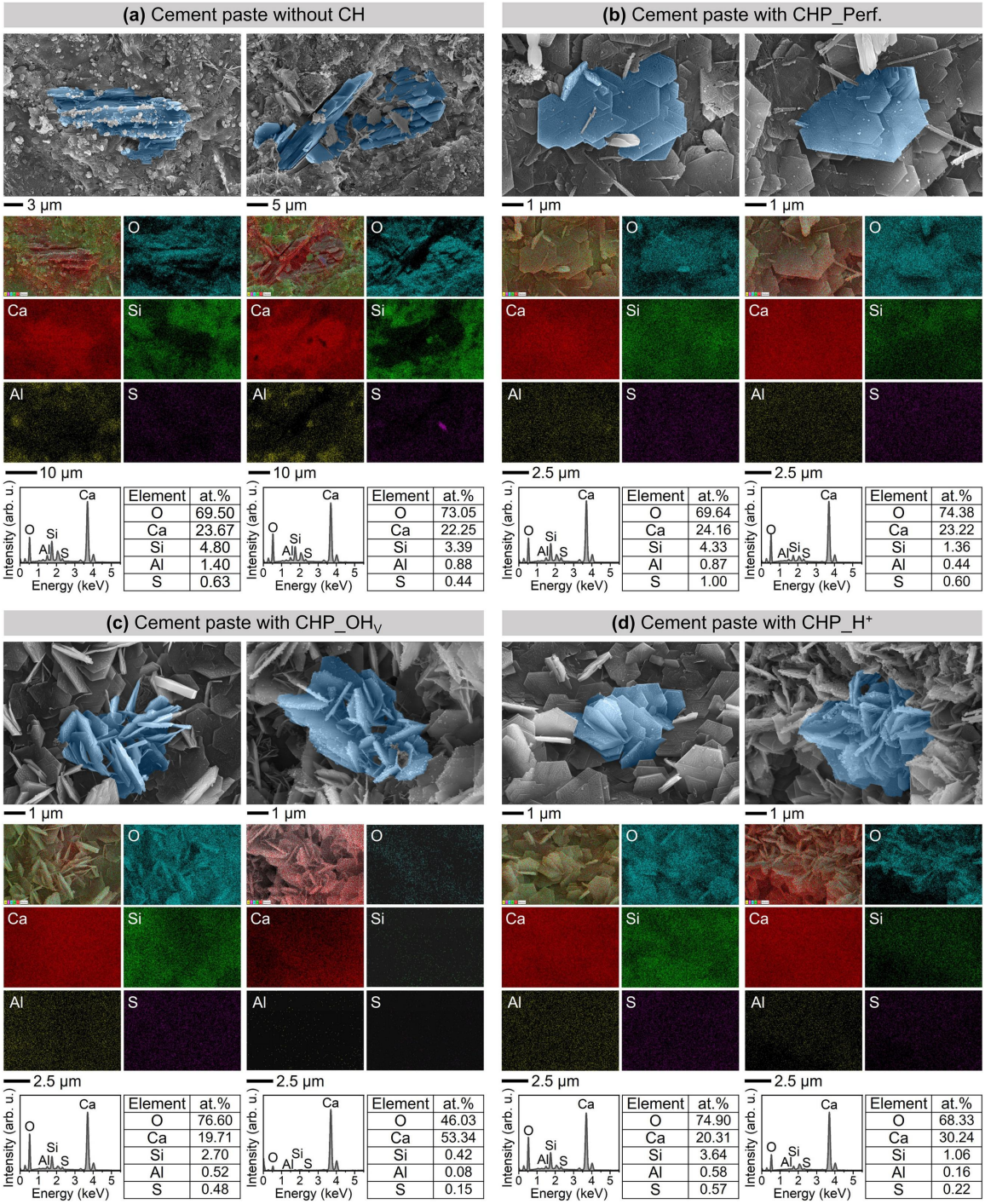
Supplementary Fig. 21 | The proportion of each phase component, based on the deconvoluted results of theoretical frequency counts. (a) Cement paste without CHP. (b) Cement paste with CHP_Perf. (c) Cement paste with CHP_OH_V. (d) Cement paste with CHP_H^+. Source data are provided as a Source Data file.

Note: The quantitative discrepancy between nanoindentation and TG/QXRD results arises from inherent differences between the two techniques, which provide complementary rather than contradictory information for cement-based material characterization. Specifically, they differ in physical meaning: nanoindentation yields volume fractions of mechanical phases via local micromechanical response, while TG/QXRD measures mass fractions of bulk crystalline phases [3, 4]. They also have complementary phase identification capabilities and observation scales, with nanoindentation distinguishing various C-S-H gels but underestimating CH content from invalid pore-region data, while TG/QXRD accurately quantifies crystalline phases at the macroscopic bulk scale but fails to identify amorphous phases such as C-S-H. In addition, as this study primarily aims to explore the effect of CHP on the mechanical properties of C-S-H gel, macropores and unhydrated clinker-enriched regions were excluded from all indentation test areas to ensure sufficient valid data points.

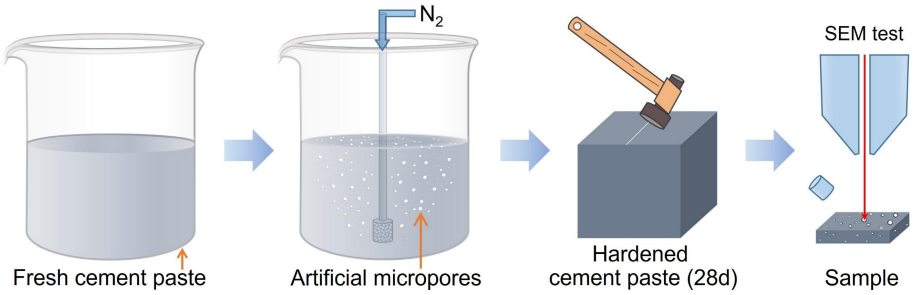


Supplementary Fig. 22 | Growth rate of compressive strength. (a) Cement pastes with different water-cement ratios at 28 days. (b) Cement pastes at different curing ages with w/c=0.35. Experiments were independently repeated 6 times with similar results. Source data are provided as a Source Data file.

Note: The hydration reaction of cement is ultimately limited by available space and water [5, 6]. Once the space is sufficiently filled with hydration products and pore water is largely depleted, the hydration reaction enters a plateau stage, during which the increases in both hydration product content and strength nearly stagnate. Accordingly, w/c = 0.35 and curing age = 28 d were selected, as the compressive strength difference between the CHP_H^+ group and the group without CHP was only 6.9%. Samples with w/c = 0.3 were excluded due to poor workability.

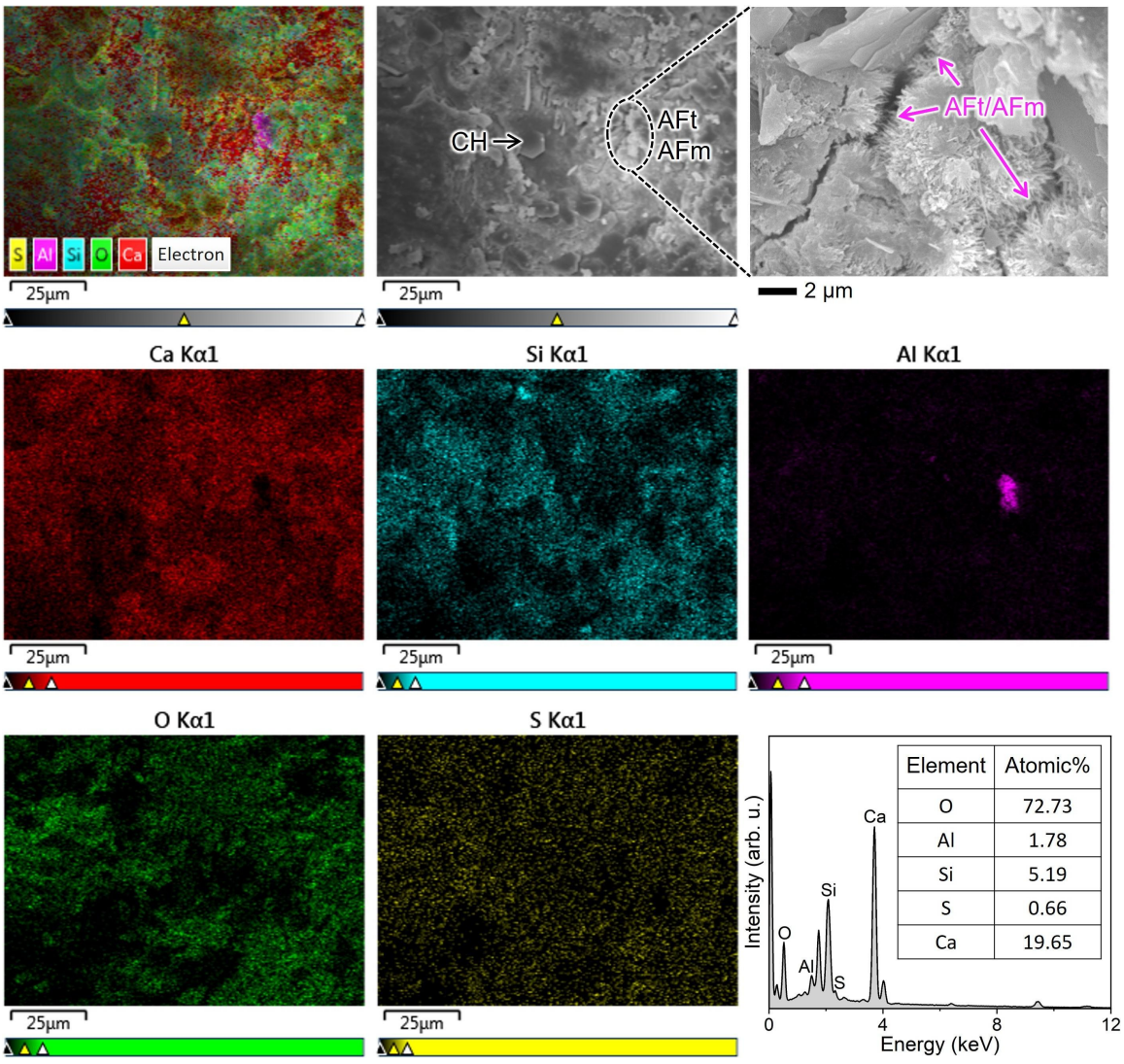


Supplementary Fig. 23 | SEM-EDS surface scan images and element distribution maps of CH in conventional cement paste at 28 days. (a) Cement paste without CHP. (b) Cement paste with CHP_Perf. (c) Cement paste with CHP_OH_V. (d) Cement paste with CHP_H^+. The blue area represents CH.



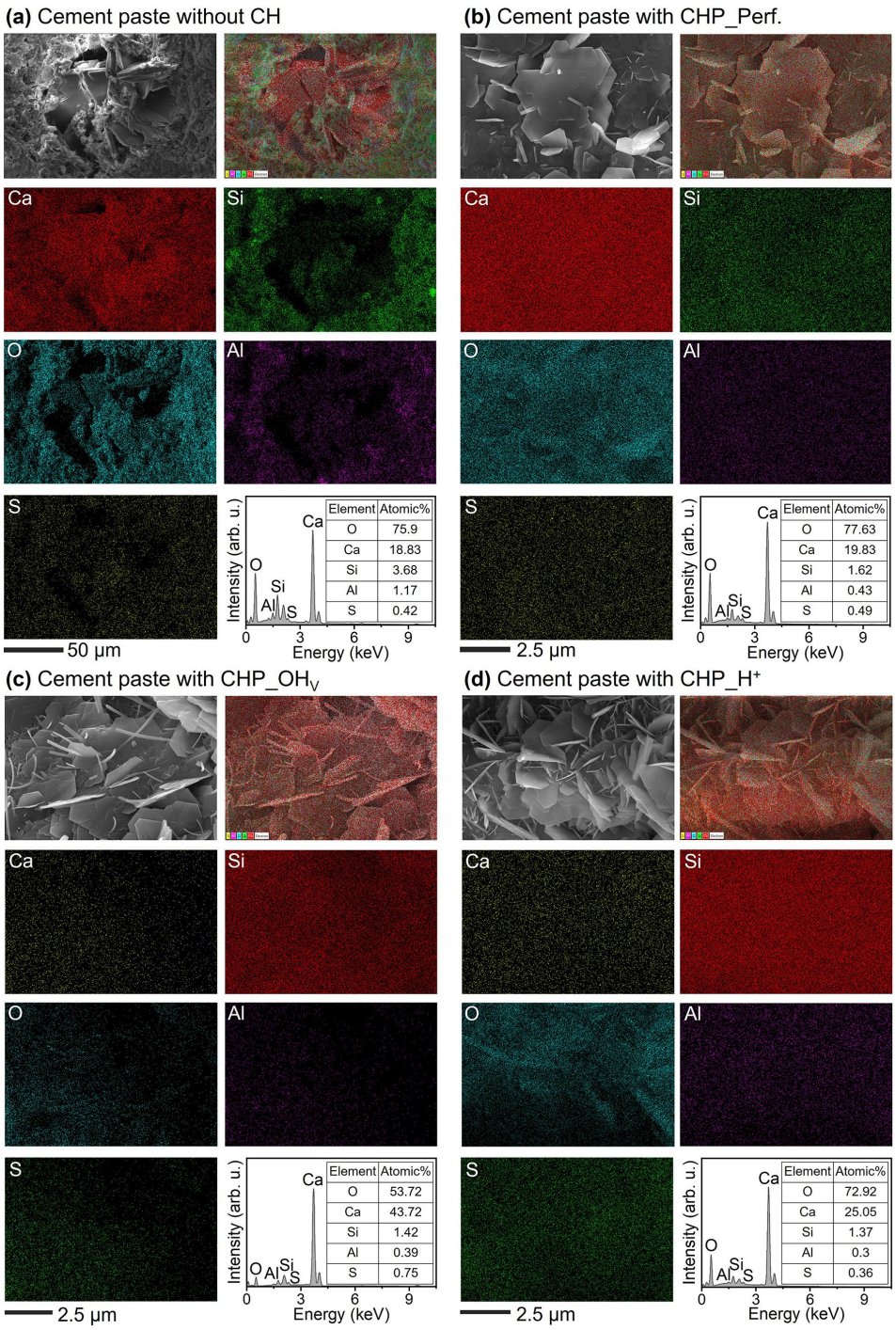
Supplementary Fig. 24 | Preparation process for cement paste with reserved artificial micropores. Fine N_2 gas was injected into the fresh samples during stirring to reserve artificial micropores. After 28 days of curing, the samples were split into smaller pieces for SEM testing.

Note: Direct characterization of CH morphology within the cementitious matrix is inherently compromised by mechanical sample preparation. Sectioning and polishing inevitably disrupt the delicate CH lamellae encapsulated within the C-S-H gel, leaving intact morphology observable only within fortuitously exposed natural micropores or microcracks. However, the stochastic distribution and variable dimensions of these natural voids preclude systematic, reproducible observation and introduce significant sampling bias. Therefore, we adopted the method shown in Supplementary Fig. 24 to induce fine and uniform artificial micropores. This method does not create non-existent CH; instead, it provides a stable “observation window” for reproducible and traceable characterization of CH.

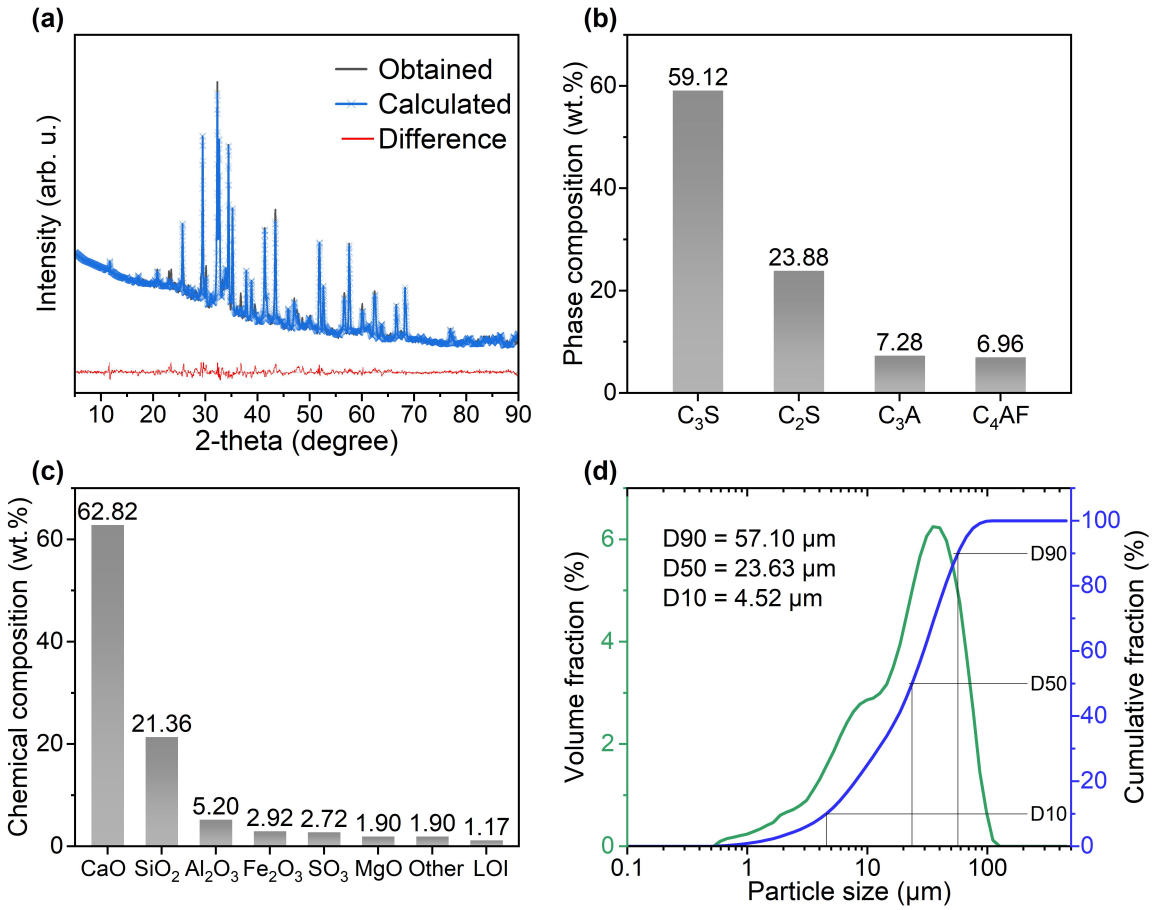


Supplementary Fig. 25 | SEM-EDS surface scan images and element distribution maps of AFt/AFm and CH in cement paste at 28 days. Experiments were independently repeated 3 times with similar results.

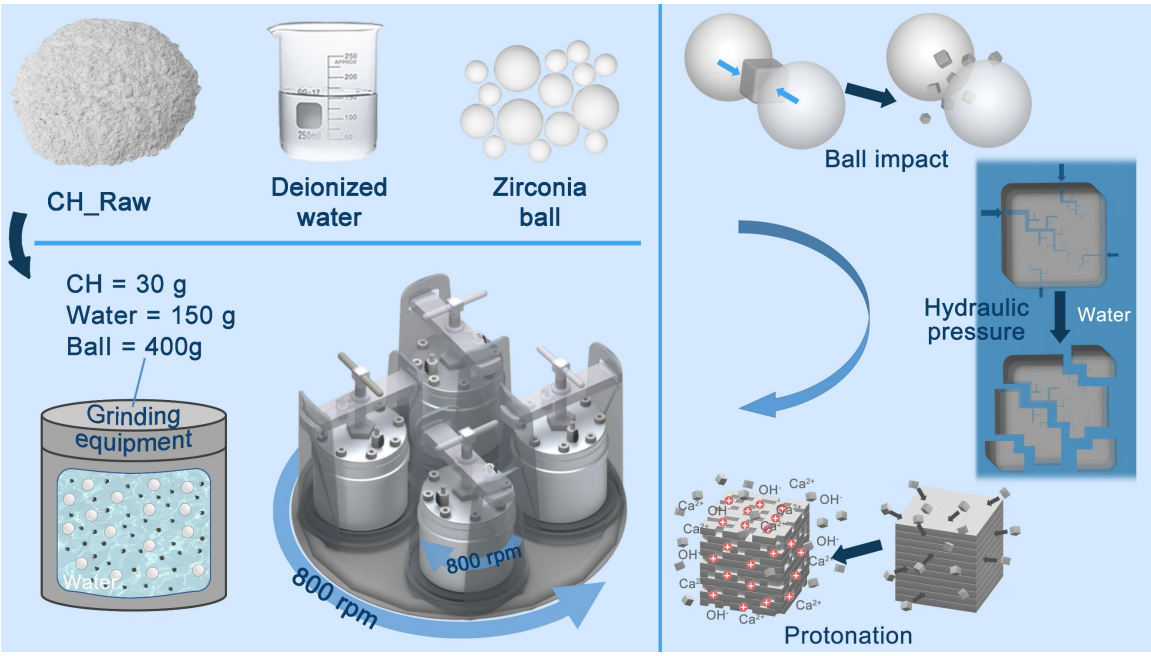
Note: AFt/AFm in cement hydration products are mainly rod-shaped or needle-shaped, while CH exhibits a hexagonal plate-like morphology [7, 8]. AFt and AFm correspond to $3CaO{\cdot}Al_2O_3{\cdot}3CaSO_4{\cdot}32H_2O$ and $3CaO{\cdot}Al_2O_3{\cdot}CaSO_4{\cdot}12H_2O$, respectively, and Ca, O, Al, and S are detectable in their EDS spectra.



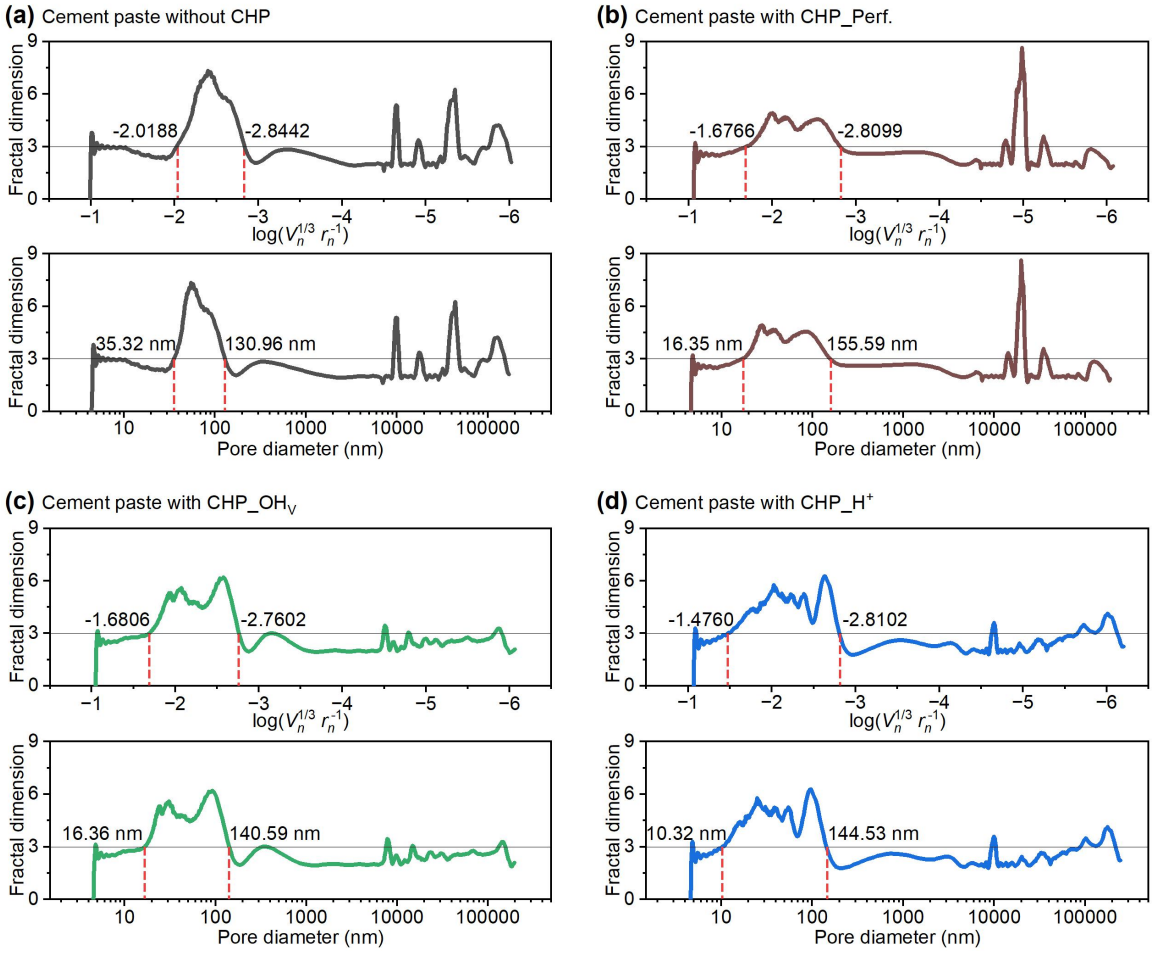
Supplementary Fig. 26 | SEM-EDS surface scan images and element distribution maps of CH in cement paste containing artificial micropores at 28 days. (a) Cement paste without CHP. (b) Cement paste with CHP_Perf. (c) Cement paste with CHP_OH_V. (d) Cement paste with CHP_H^+. The preparation of samples with artificial micropores is referenced in Supplementary Fig. 24. Experiments were independently repeated 3 times with similar results.



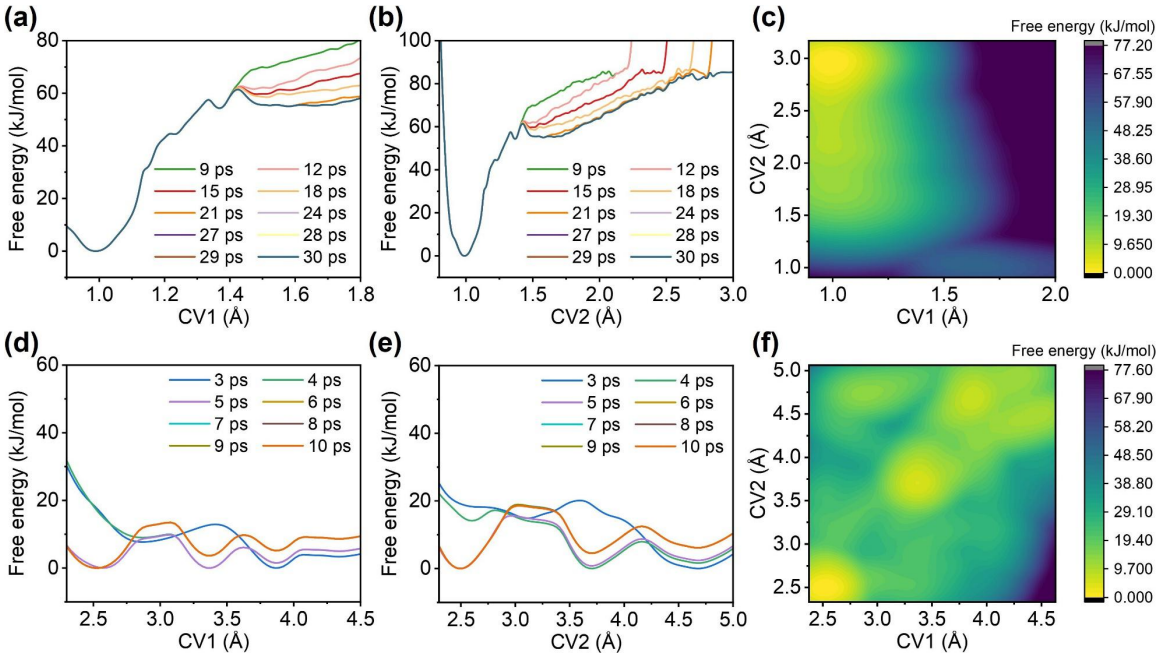
Supplementary Fig. 27 | Characterisation of Ordinary Portland cement (P.O. 42.5 type). (a) X-ray diffraction (XRD) patterns. (b) Phase composition. C_3S, C_2S, C_3A and C_4AF denote tricalcium silicate ($3CaO{\cdot}SiO_2$), dicalcium silicate ($2CaO{\cdot}SiO_2$), tricalcium aluminate ($3CaO{\cdot}Al_2O_3$) and tetracalcium aluminoferrite ($4CaO{\cdot}Al_2O_3{\cdot}Fe_2O_3$), respectively. (c) Chemical composition. (d) Particle size distribution. Source data are provided as a Source Data file.



Supplementary Fig. 28 | Preparation process of CHP_H$^+$ and schematic diagram of wet grinding process. The left part shows the wet ball-milling process for synthesizing CHP_H$^+$, clearly indicating the fixed amounts of the CH_Raw, deionized water, and zirconia ball. The right part illustrates the evolution of CH, including the crushing of CH due to mechanical impact, further breakdown of CH by water pressure in turbulent flow, the formation of lattice defects in CH, and subsequent protonation.



Supplementary Fig. 29 | Relationship between fractal dimension and log($V_n^{1/3}$ r_n^{-1}), and relationship between fractal dimension and pore diameter. (a) Cement paste without CHP. (b) Cement paste with CHP_Perf. (c) Cement paste with CHP_OHv. (d) Cement paste with CHP_H^+. The data in Fig. 6e were differentiated to the first order, and D = 3 was used as the boundary for dividing different fractal regions. Source data are provided as a Source Data file.



Supplementary Fig. 30 | Convergence of the metadynamics simulations. (a) and (b) Time-evolution free energy profiles of (a) CV1 (Å) and (b) CV2 (Å) of perfect CH during protonation. (c) 2D free energy surfaces at 30 ps of perfect CH during protonation. (d) and (e) Time-evolution free energy profiles of (d) CV1 (Å) and (e) CV2 (Å) of CH with OH vacancy during protonation. (f) 2D free energy surfaces at 10 ps of CH with OH vacancy during protonation. The perfect CH (a and b) exhibits a constant curve in the range of 24 ps to 30 ps, while the CH with OH vacancy (d and e) shows a constant curve of 6 ps to 10 ps. Source data are provided as a Source Data file.

Supplementary References

1. He, Z.-T. et al. Thermodynamic analysis of adsorption transitions in porous adsorbents from surface adsorption to capillary condensation. *Separation and Purification Technology* **394**, 137434 (2026).

2. Marbán, G. BET adsorption reaction model based on the pseudo steady-state hypothesis for describing the kinetics of adsorption in liquid phase. *Journal of Colloid and Interface Science* **467**, 170-179 (2016).

3. Zhang, Z. et al. Comparison of three different deconvolution methods for analyzing nanoindentation test data of hydrated cement paste. *Cement and Concrete Composites* **138**, 104990 (2023).

4. Liu, Y. et al. Multi-scale creep analysis of cement paste – Indentation prediction and time correspondence of mechanisms. *Cement and Concrete Composites* **134**, 104815 (2022).

5. Scrivener, K. et al. Advances in understanding cement hydration mechanisms. *Cement and Concrete Research* **124**, 105823 (2019).

6. Bullard, J. W. et al. Mechanisms of cement hydration. *Cement and Concrete Research* **41**, 1208-1223 (2011).

7. Wang, H. et al. Contributions of ettringite, C-S-H, and free water to shotcrete's mechanical properties: Implications from equivalent cement pastes. *Cement and Concrete Research* **196**, 107927 (2025).

8. Nelson, S. et al. Development of calcium sulfoaluminate-belite cements for the encapsulation of radioactive waste. *Cement and Concrete Composites* **165**, 106355 (2026).